Journal Pre-proof

Effect of heat treatment on erosion–corrosion of Fe-based amorphous alloy coating under slurry impingement

Fei Huang, Jia-jie Kang, Wen Yue, Xiao-bin Liu, Zhi-qiang Fu, Li-na Zhu, Ding-shun She, Guo-zheng Ma, Hai-dou Wang, Jian Liang, Wei Weng, Cheng-biao Wang

This is a PDF file of an article that has undergone enhancements after acceptance, such as the addition of a cover page and metadata, and formatting for readability, but it is not yet the definitive version of record. This version will undergo additional copyediting, typesetting and review before it is published in its final form, but we are providing this version to give early visibility of the article. Please note that, during the production process, errors may be discovered which could affect the content, and all legal disclaimers that apply to the journal pertain.

Author Contributions Section

Fei Huang: Methodology, Formal analysis, Investigation, Writing-Original Draft, Writing-Review & Editing. **Jiajie Kang**: Conceptualization, Methodology, Resources, Writing-Review & Editing, Project administration. **Wen Yue**: Conceptualization, Methodology, Resources, Project administration. **Xiaobin Liu**: Validation, Investigation. **Zhiqiang Fu**: Resources, Methodology. **Lina Zhu**: Methodology, Formal analysis. **Dingshun She**: Methodology, Formal analysis. **Guozheng Ma**: Resources, Supervision. **Haidou Wang**: Resources, Supervision. **Jian Liang**: Validation, Investigation. **Wei Weng**: Validation, Investigation. **Chengbiao Wang**: Project administration, Conceptualization.

Effect of Heat Treatment on Erosion–corrosion of Fe-based Amorphous Alloy Coating under Slurry Impingement

Fei Huang[1], Jia-jie Kang[1,2,4*], Wen Yue[1,2,4*], Xiao-bin Liu[1], Zhi-qiang Fu[1,4], Li-na Zhu[1,4], Ding-shun She[1,4], Guo-zheng Ma[3], Hai-dou Wang[1,3], Jian Liang[5], Wei Weng[6], Cheng-biao Wang[4,7]

(1. School of Engineering and Technology, China University of Geosciences (Beijing), Beijing 100083, PR China;

2. Key Laboratory of Deep GeoDrilling Technology of Ministry of Natural Resources, Beijing 100083, China

3. National Key Lab for Remanufacturing, Academy of Armored Forces Engineering, Beijing 100072, China

4. Zhengzhou Institute, China University of Geosciences (Beijing), Zhengzhou 451283, China

5. Institute of Exploration Techniques, Chinese Academy of Geological Sciences, Langfang 065000, PR China;

6. Beijing Institute of Exploration Engineering, Beijing 100083, PR China)

7. Zhengzhou Institute of Multipurpose Utilization of Mineral Resources, Chinese Academy of Geological Sciences, Zhengzhou 450006, China

Corresponding author: kangjiajie@cugb.edu.cn (Jia-jie Kang) cugbyw@163.com (Wen Yue)

Abstract: In order to investigate the effect of vacuum heat-treatment (VHT) on the erosion–corrosion performance of Fe-based amorphous alloy coating (Fe-AAC) under alkaline sand-containing NaCl slurry impingement, $Fe_{48}Cr_{15}Mo_{14}C_{15}B_6Y_2$ at.% amorphous alloy coatings were first prepared via a high-velocity air fuel (HVAF) spraying process and then vacuum heat-treated at several different temperatures. Experimental results show that the fraction of the amorphous phase in the coating decreases with increasing VHT temperature. The heat-treated coatings exhibit a higher hardness of ~994 $HV_{0.1}$ with good wear resistance

but lower corrosion potentials of ~-0.607 V and a larger corrosion current density of ~7.98 $\times$ 10^{-6} A. Erosion−corrosion tests show that the mass loss increases as the temperature of the heat-treatment increases under the same conditions of slurry pH. However, as the slurry pH values increase, the mass loss of the sample treated at the same VHT temperature tends to decrease. The mechanism of erosion−corrosion failure of the Fe-AAC is the synergy of wear by fluidity particles on coatings and corrosion of corrosive media during erosion.

Key words: Fe-based amorphous alloy; Coating; High-velocity air fuel spraying (HVAF); Crystallization; Wear; Erosion-corrosion

1. Introduction

Fe-based amorphous alloys are characterized by short-range order, long-range disorder, and the absence of crystal defects such as grain boundaries and dislocations, which make them have higher strength and excellent anti-corrosion and wear-resistance properties [1−4]. In order to expand the application field of them and reduce costs, an effective way to prepare them into coatings is by thermal-spraying processes such as high-velocity air fuel (HVAF). Nowadays, Fe-based amorphous alloy coatings (Fe-AACs) are becoming a promising metallic material with a wide range of application prospects, such as biomedical materials, vehicles, watercraft, and within nuclear industry under the research of many predecessors [5−7]. Zohdi et al. investigated the corrosion behavior of $Fe_{55−X}Cr_{18}Mo_7B_{16}C_4Nb_x$ (x = 0, 3, and 4 at.%) amorphous alloy in Ringer's solution with a pH value 6.5 and open to air at 37°C to estimate the feasibility of Fe-based amorphous alloy as potential biomaterials used in the human body. They showed excellent corrosion resistance compared to Ti-6Al-4V and no ion release, implying that these alloys could be applied as biomaterials [8]. Yao et al. reported that

2

$Fe_{59}Cr_{12}Nb_5B_{20}Si_4$ HVOF-sprayed coating could be an available and proper candidate for metal-based thermal barrier coating application in vehicle engines where heat protection and associated wear resistance are simultaneously required [9]. Guo et al. showed that $Fe_{49.7}Cr_{18}Mn_{1.9}Mo_{7.4}W_{1.6}B_{15.2}C_{3.8}Si_{2.4}$ amorphous coating combines high boron content and good corrosion and wear resistance. It is promising for underground applications, especially the storage of spent nuclear fuels [10].

Among the above-mentioned applications, the hardness and corrosion resistance of the coatings are very important indicators. For further improving these two indicators, many efforts have been made by predecessors. The main factors affecting corrosion resistance and hardness are the composition and structure of the coatings [11−14]. Elements, such as Cr, Mo, and Ni, are inherently resistant to corrosion, which prevents the corrosion of the coatings by a mechanism that rapidly forms an oxide film during the corrosion process. Also, their addition makes the composition of the coatings more complicated, which makes the formation of the amorphous phase easier during the spraying process, and further improves the corrosion resistance of the coatings [11, 15]. Research have also showed that the coatings with amorphous/crystalline composite structure prepared by heat treatment have higher hardness due to the dispersion strengthening of nanocrystals and the barrier effect of grain boundary on dislocation [16−18]. However, defects, such as pores and cracks, caused by improper selection of spray parameters can significantly deteriorate the corrosion resistance and hardness of the coating [19, 20].

During the drilling process, where the operating environment is similarly harsh, alkaline NaCl-containing drilling fluid is used to maintain the stability of the drilling hole and the

drilling efficiency. The fluid carrying the rock debris during the drilling process becomes slurry, causing the erosion−corrosion behavior, which combines the actions of mechanical wear and chemical corrosion [21, 22]. This phenomenon exists in the mechanical overflow parts such as oil and gas pipelines and water pumps. Erosion−corrosion causes low mechanical efficiency, short service life, and seriously affects the stability and safe operation of the drilling unit. Therefore, drilling equipment has a great demand for coatings having excellent erosion resistance. Actually, Fe-AACs still have theoretical advantages in application, but there is limited related research.

In the present work, $Fe_{48}Cr_{15}Mo_{14}C_{15}B_6Y_2$ (at.%) amorphous alloy coatings were prepared by HVAF for conducting sand-containing slurry impingement experiments. Simulating drilling slurry with several controlled pH values was also prepared to investigate the effect of alkalinity in the slurry on the erosion−corrosion resistance of the coatings. At the same time, in order to verify whether the heat treatment has the possibility of enhancing the erosion−corrosion resistance, several different temperatures of VHTs were applied to Fe-AACs as-sprayed. The micro-structural characteristics, wear behavior, and electrochemical corrosion behavior of the heat-treated Fe-AACs were investigated. The mechanism of the influence of alkaline environment and VHT on erosion−corrosion of Fe-AACs under sand-containing slurry impingement was also discussed.

2. Experiment

2.1 Coating preparation and heat treatment

$Fe_{48}Cr_{15}Mo_{14}C_{15}B_6Y_2$ (at.%) amorphous alloy powders prepared by argon gas atomization with a size range of 25–58 μm were screened out as the feedstock powders for spraying. The Fe-based powders were then thermally sprayed on 35CrMo steel substrates with a size of 50 mm × 15 mm × 5 mm by an HVAF thermal-spraying system with an AK06-2#

spraying gun (Kermetico, USA). Table 1 summarizes the detailed spraying parameters. Before thermal spraying processing, the steel substrates were cleaned by acetone, dried in air, and then grit blasted with commercial alumina to obtain appropriate surface roughness. The substrates are preheated one back and forth at a preheating speed of 0.8 m/s. Then, alumina particles (45–75 μm) at a volume ratio of 1:1 were added in feedstock to avoid blocking the nozzle, and it has also been proved that alumina particles can increase the impact effect of droplets to make coating denser [23] and also has less influence on the corrosion resistance of the coating in sodium chloride solution [24].

Before the erosion–corrosion test, the as-sprayed coatings were subsequently heat treated in a vacuum annealing furnace at 600°C, 700°C, and 800°C for 1 h and then subjected to furnace cooling. T600, T700, and T800 are, respectively, used to abbreviate the heat-treated coatings. The temperatures of VHT are based on the crystallization temperature of amorphous phase.

Table 1 Spraying parameters employed in the HVAF process

Factor	Parameters
Gun	AK06-2#
Compressed air flow (psi)	91
Propane flow (psi)	100
Nitrogen flow(L/min)	22
Hydrogen flow(L/min)	30
Spraying distance (mm)	200
Feed rate (g/min)	100
Traverse velocity (mm/s)	500

2.1 Characterization of the coating

5

Scanning electron microcopy (SEM, MERLIN Compact, ZEISS, Germany) coupled with Energy Dispersive Spectrometer (EDS, Ultim, Oxford, England) was used to examine and analyze the morphology, microstructure, and components of the powders and Fe-AACs. Transmission electron microscopy (TEM, JEM-2100F, JEOL, Japan) was carried out to take bright-field images and selected area electron diffraction (SAED) patterns to further analyze the amorphous phase and crystalline phase in coatings. The preparation of TEM samples involved firstly peeling the coating from the substrate by mechanical method and then polishing the coating to about 50 μm, then finally thinning them by the ion-beam milling technique until perforation formation.

The phase compositions of Fe-AAC before and after VHT were investigated by an X-ray diffractometer (XRD, D/max-2500V, Rigaku, Japan) with Cu Kα radiation source at a speed of 4º/min from 20º to 80º.

A Vickers-hardness tester (MICROMET-6030, Buehler, America) was used to measure the hardness values of the Fe-AAC before and after VHT with a load of 1 N and a dwell time of 10 s. Five measurements were repeated for each sample to ensure the reliability of the values.

The thermal behavior of the powders and the Fe-AAC was examined by differential thermal analysis (DTA, STA499F3, NETZSCH, Germany) at a rate of 20 K/min with continuous heating mode in a flow of argon atmosphere.

2.2 Wear test

Wear tests were conducted on a ball-on-disc wear tester (MS-T3000, Huahui, China). The counter body was Si_3N_4 with a diameter of 6 mm, which has a hardness of 1600 HV (similar with hard silicified rocks). In the dry sliding wear test of coatings, the normal load is 10 N and the rotating speed is 200 r/min (linear gliding speed is 0.0628 m/s). The test duration was 30 min (113.1 m), and all of these tests were repeated three times to ensure the reliability

6

of the data.

The worn surface of the Fe-AACs was measured using 3D surface topography (NexView, ZYGO, America) to characterize the wear volume. The morphologies and tribochemistry reaction products of the wear tracks were observed using SEM coupled with EDS.

2.3 Electrochemical measurements

Corrosion resistance properties and behavior of the Fe-AACs before and after VHT were evaluated from the polarization curves on a Potentiostat/Galvanostat (Elektrik IM6, ZAHNER, Germany) in 3.5 wt.% NaCl solution at 298 K in atmosphere environment. Electrochemical measurements were conducted in a three-electrode cell. The counter electrode used was platinum, and the counter electrode was a saturated calomel reference electrode (SCE). The coating samples used as the working electrode were polished by diamond paste to a mirror finish and closely sealed with ethylene-vinyl acetate copolymer (EVA) resin, only leaving an area of 1 cm^2 exposed. Before the electrochemical measurements, samples were immersed for several minutes, when the open-circuit potential (OCP) became steady. The scanning speed was 10 mV/min. The good reproducibility was ensured by repeating each test three times.

2.4 Erosion−corrosion test

Erosion−corrosion resistance of the Fe-AACs was carried out using an erosion−corrosion tester (MLD-10, Jnyihua, China), as shown in Fig. 1. The specimens were fixed on an axis of rotation with a speed of 200 r/min, and the linear velocity at the mid-plate position was 1.68 m/s. The slurry consisted of 45 vol.% quartz particles (1–2 mm) and 3.5 wt.% NaCl solution. The pH values of the slurry were set at 7, 9, and 11 by adding sodium hydroxide to simulate varying degrees of alkaline environment. Before the erosion-corrosion test, the specimen surfaces were polished with 1500 grid diamond paste, then cleaned in alcohol and dried in air. After erosion-corrosion for 4 h, the specimens were degreased, rinsed, dried, and finally weighted using an analytical balance with an accuracy of 0.1 mg. Each test was repeated at

7

least three times to get reliable results.
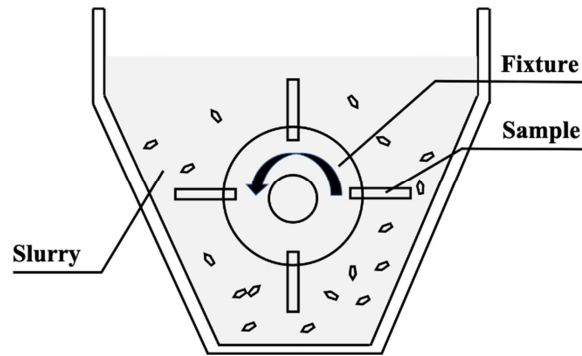
Fig. 1 Schematic of MLD-10-type erosion–corrosion tester

3. Result and Discussion

3.1 Characterization of coatings

Figure 2 shows the SEM micrographs and XRD pattern of Fe-based amorphous feedstock powders and as-sprayed coating. The powder is spherical and the surface is smooth, which gives better flowability when sprayed. After spraying, an Fe-AAC with a thickness of about 280 μm was formed on the 35CrMo steel substrate. The surface of the coating has a large roughness, due to the distribution of the flattened structure formed by the cooling of the droplets. XRD patterns of both feedstock powders and Fe-AACs exhibit a broad halo peak at $2\theta = 40–50°$, but there are also some crystalline peaks, which mean that the powders and coating are not completely amorphous. The results show that the corresponding components of the crystal phase in the powders are mainly α-Fe, iron carbide, and iron molybdenum. For the coating, the peaks of alumina are very strong due to the addition of Al_2O_3 particles. Furthermore, some crystalline peaks in the feedstock powders disappear in the coating, indicating that the thermal spraying process promotes the transformation of crystal phase to amorphous, due to the molten particles obtaining a rapider quenching rate in the HVOF process than argon gas atomization through the action of flattening onto the substrate surface [25].

8
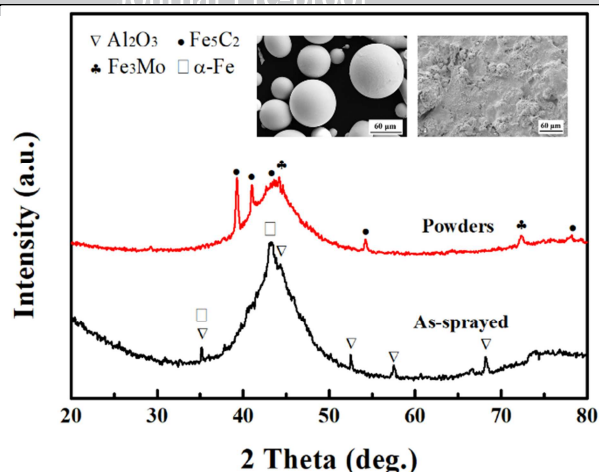
Fig. 2 Microstructure and XRD pattern of feedstock powders and as-sprayed coating

The bright-field TEM image and selected area electron diffraction (SAED) patterns of the as-sprayed Fe-AAC are shown in Fig. 3. The diffused halo rings in the selected area diffraction pattern indicate that the coatings are basically composed of the amorphous phase. Moreover, the diffraction spots validate the existence of crystals, which further confirm that the coating was not completely amorphous, which was consistent with that of the XRD results. Crystallization in the as-sprayed coatings is mainly related to the localized reheating that occurs when the coatings are deposited in a layer-by-layer manner [26].
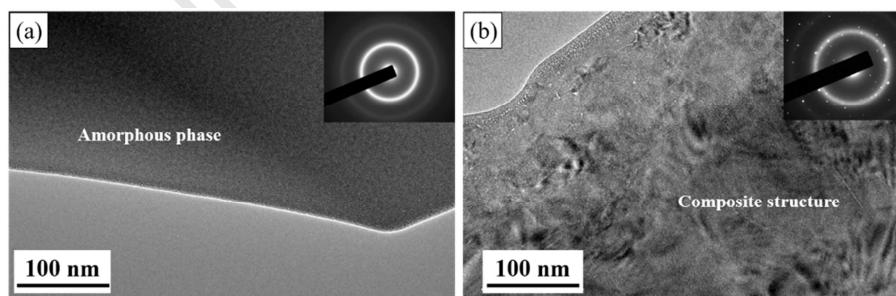
Fig. 3 Bright-field TEM image and selected area electron diffraction (SAED) patterns of the as-sprayed coating

Figure 4 shows the DTA curves of powders and as-sprayed coating. They show the same exothermic reaction, indicating a crystallization onset temperature of 677–679°C. This means that the Fe-AAC will crystallize when the VHT temperature exceeds the crystallization onset temperature. This provides a basis for setting the VHT temperature of the coating.
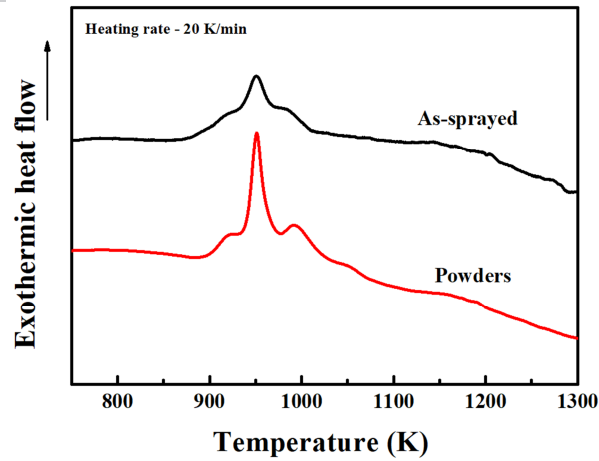
Fig. 4 DTA curves of powders and as-sprayed coating
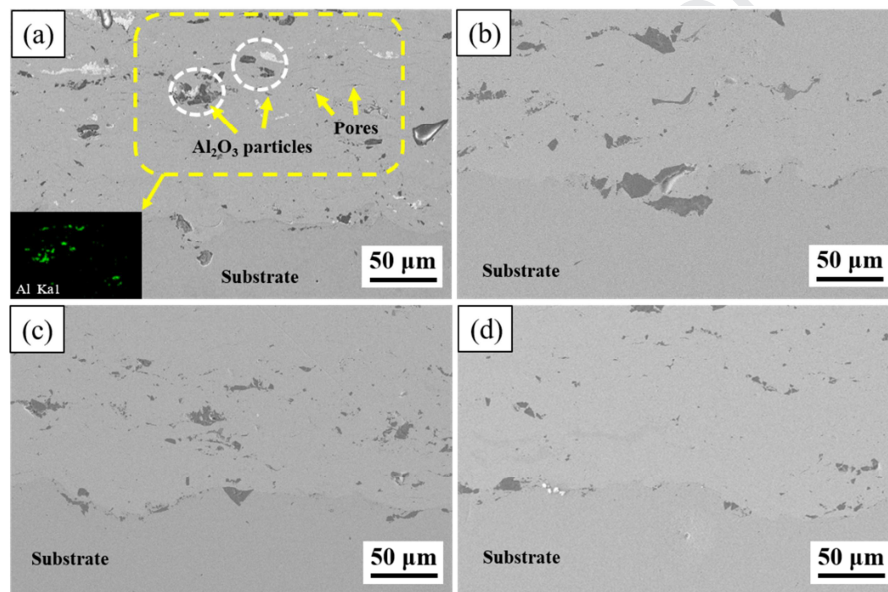
Fig. 5 SEM images of cross-sections of the heat-treated coatings at different temperatures: (a) as-sprayed, (b) T600, (c) T700 and (d) T800.

SEM images of cross-sections of the as-sprayed and heat-treated Fe-AACs at different temperatures are shown in Fig. 5. It can be found that there are particulate structures in the coating, which are dark and unevenly distributed. From the EDS result, the big dark particulate structures are Al_2O_3 particles and the small ones are pores. The porosity of the coating after heat treatment tends to decrease, and this result has also been reported in other studies [27, 28]. There are two possibilities to reduce the porosity of the coating caused by heat treatment. One is a self-fluxing reaction caused during heat treatment [27]. The other is related to the phase transformation, in which the growth or difference degree of expansion of

10

new phases may affect porosity [28].

Figure 6 shows the XRD pattern of the as-sprayed and heat-treated Fe-AACs. It is found that the XRD patterns of the as-sprayed coating and heat-treated coatings under 800°C all show a broad halo at $2\theta = 40-50°$, indicating that the amorphous structure in these coatings is within the resolution of XRD. With the increase of temperature, the area of diffuse scattering peaks is further reduced, and the curve becomes sharper. For T800 coating, the diffuse scattering peaks almost disappear, which means that a large number of crystalline phases are formed. From the pattern, it can be concluded that crystallization behavior occurs at a heat treatment temperature of 700°C. T700 can keep a majority of amorphous structure. For T800, the crystalline phases appear in large quantities, and the major crystalline phases in the coating are composed of $Fe_{23}(C, B)_6$, $Fe_{17}Y_2$, Al_2O_3, $Al_{13}Fe_4$, and α-Fe.
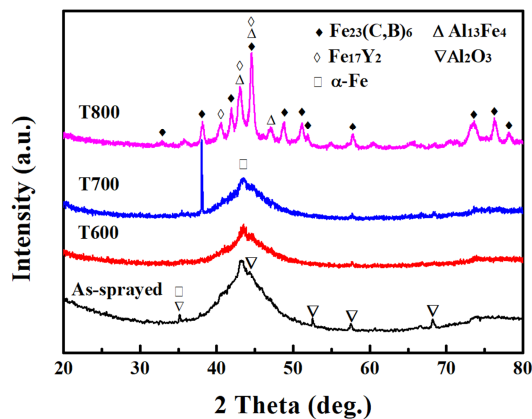
Fig. 6 XRD pattern of the as-sprayed and heat-treated coatings

The Vickers microhardness of the as-sprayed and heat-treated Fe-AACs is presented in Fig. 7. In general, all of the heat-treated coatings are harder than the as-sprayed coating (746 ± 55 $HV_{0.1}$). Several studies have shown that the microhardness changing with the heat treatment temperatures can be classified into distinct stages as follows: initially, the hardness is improved because of the appearance of nanocrystals dispersed in the amorphous phase; then, the more nanocrystals makes the hardness continue to increase [29, 30].

For T600, since the VHT temperature is lower than the crystallization onset temperature of the amorphous phase, there is no effect of crystallization in this process, and the slight increase in the hardness of the coating is mainly due to the homogenization of the coating composition caused by the VHT. This is also the reason why some crystal peaks in the XRD pattern become weak. For T700, which was treated near the crystallization onset temperature, nanocrystalline phases begin to form inside the coating. The dispersion distribution of these nanocrystalline phases, which are hardly detectable within the resolution of XRD, is the main mechanism for improving the hardness. The formation of nanocrystalline greatly increases the grain boundaries due to the Hall-Petch effect and makes the hardness of the coatings greatly improved [31]. For T800, which was treated higher than the crystallization onset temperature, the coating contains many hard phases of carbides and borides (Fig. 6). The precipitation of these hard phases and grain boundaries, which create barriers that prevent dislocation motion, is the main mechanism for improving the hardness dramatically [32].
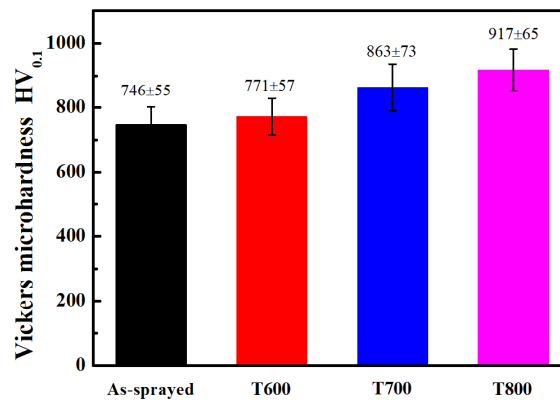
Fig. 7 Vickers microhardness of the as-sprayed and heat-treated coatings

3.2. Wear behavior

After VHT, the hardness has been improved due to the change of phases in the coatings as shown above (Fig. 6). According to the Archard equation of $Q = \frac{KWL}{H}$ [33, 34], the total volume of wear debris (Q) produced during wear is negatively correlated with the hardness of the softer contacting surface (H) at a given load (W), a constant K, and sliding distance (L).

12

Therefore, Fe-AAC after VHT with higher hardness will have better wear resistance theoretically.

The 3D topographies of typical worn surface on coatings after a wear test are shown in Fig. 8. It can be found that as the VHT temperature increases, the wear scars on the surface of the coating become shallower, which is consistent with the theory mentioned above. The wear scar formed on the coatings are rougher and presents two distinguishing zones, a dark-color zone (complete matrix) and a light-color zone corresponding to the highly-oxidized particles. The signal of oxygen is distributed throughout the wear scar and concentrated in the light areas. Combined with the SEM images and oxygen surface partial map shown in Fig. 9, it is confirmed that the wear mechanism of the coating is mainly oxidative wear. All of the coating samples have exhibited a similar wear mechanism dominated by oxidative wear. For further analysis, wear rates were also calculated.
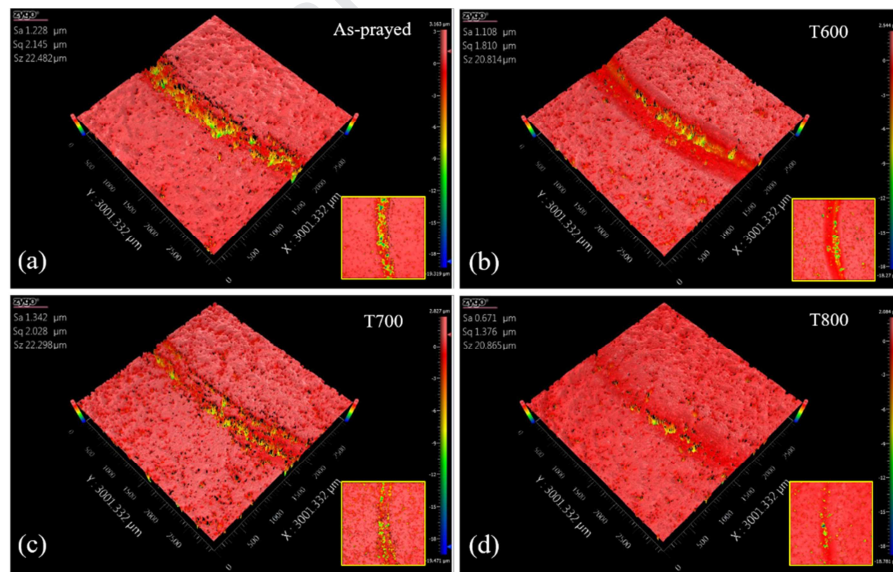
Fig. 8 3D topographies of typical worn surface on coatings after wear test: (a) as-sprayed, (b) T600, (c) T700 and (d) T800.
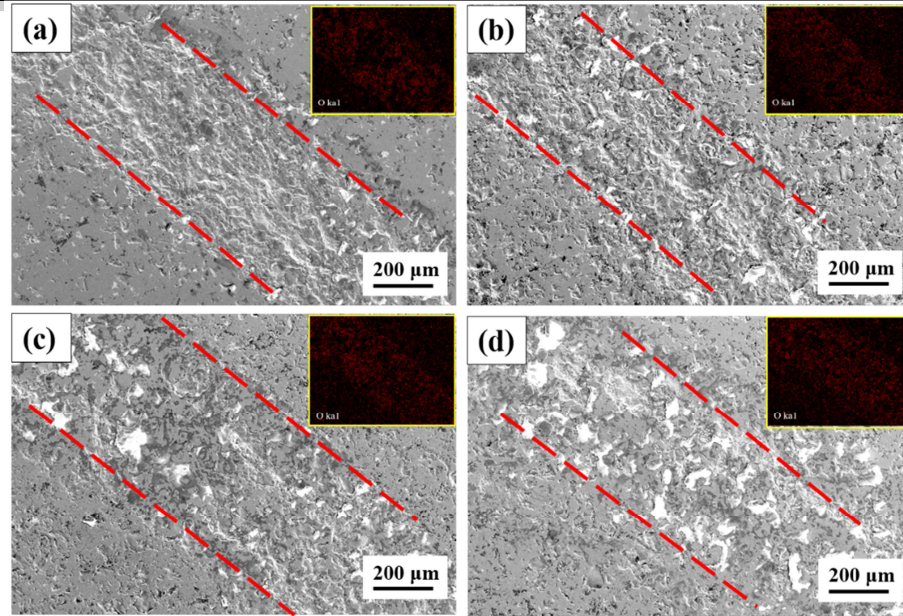
Fig. 9 SEM images and oxygen surface partial map of the worn surface on coatings: (a) as-sprayed, (b) T600, (c) T700 and (d) T800.

Figure 10 shows the wear rates of Fe-AACs after a wear test. The wear rate was calculated using the equation of $Q = \frac{V_W}{N \cdot S}$ [35], where Q is the wear rate in μm^2/ N, V_W is the wear volume (μm^3), and N and S mean the applied load (N) and the total sliding distance (μm), respectively. The wear rate of the T800 specimen is only 79 ± 4.2 μm^2/N, which is one-third of the as-sprayed coating sample (237 ± 13.8 μm^2/N), showing very good wear resistance. This can confirm that appropriate VHT can improve the wear resistance of Fe-AAC.
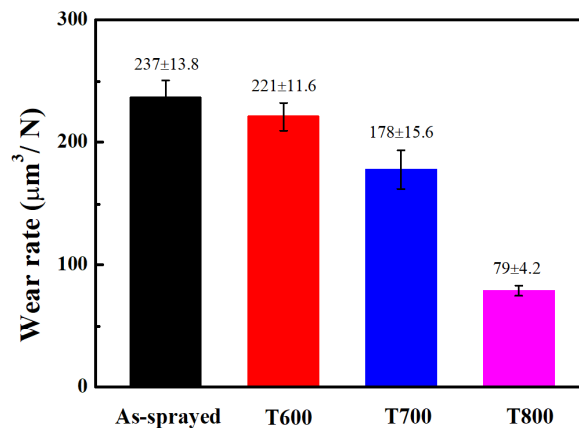
Fig. 10 Wear rates of coatings after wear test

3.3. Electrochemical corrosion behavior

Figure 11 shows the polarization curves of Fe-ACCs in 3.5 wt.% NaCl solution. The corrosion potentials of as-sprayed, T600, T700, and T800 are -0.309 V, -0.359 V, -0.475 V, and -0.607 V, respectively. The corrosion current densities are 2.32×10^{-6} A, 2.89×10^{-6} A, 3.56×10^{-6} A, and 7.98×10^{-6} A, respectively. All of the coating samples show better corrosion resistance than the substrate. On the whole, the corrosion potential decreases and the corrosion current density increases with the increasing temperature of VHT. The result shows that the corrosion resistance of Fe-AACs is getting worse. For T600, homogenization of components and the growth of the original grains after VHT have negative effects on the corrosion resistance, which makes the heat-treated coating have lower corrosion potential and higher corrosion current densities than the as-sprayed sample. For T700 and T800, the corrosion current density increases rapidly in the process of electrochemical corrosion. It can be seen that the transformation of the amorphous phase into the crystalline phase causes the decrease of the corrosion resistance. The main reasons for deterioration of corrosion resistance are due to the grain growth and crystallization [36]. Crystallization can increase the number of grain boundaries, which makes more channels for chloride ions entering into the interior of the coating to cause serious damage.
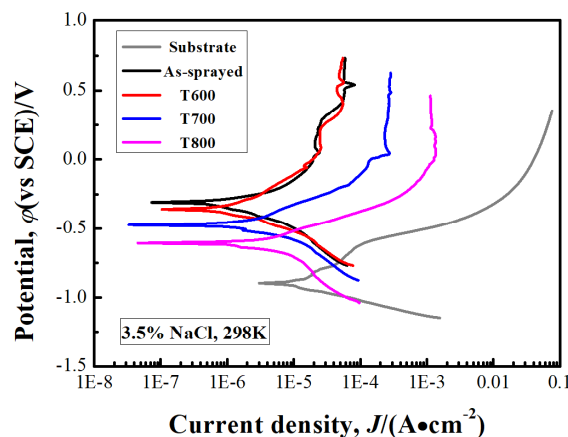
Fig. 11 Potentiodynamic polarization curves of coatings in 3.5 wt.% NaCl solution

3.4. Erosion-corrosion behavior

The mass loss and SEM images of the substrate, as-sprayed, and heat-treated coatings after erosion-corrosion tests in alkalinity sand-containing NaCl slurry are shown in Figs. 12 and 13, respectively. Under the same conditions of slurry pH, the mass loss increases as the temperature of the VHT increases. Nevertheless, the mass loss of the coating is much smaller than that of the 35CrMo substrate after an erosion-corrosion test. It can also be found that as the pH values increase, the mass loss of the coating treated at the same temperature tends to decrease.

The damage of coatings shown in Fig. 13 is consistent with the change of mass loss (Fig. 12). After the erosion-corrosion tests, the surface of the specimens suffered from various degrees of damage, such as cracking and spalling of the coating. Due to the low hardness and corrosion resistance, severe scratches and corrosion products appear on the surface of the substrate. For the coatings, the T800 coating tested in pH = 7 slurry suffered the most serious damage. The damage is caused by the physical impact of the quartz particles in the slurry and the chemical corrosion of chloride ions. These two processes promote each other in the destruction of coatings. The corrosion of chloride ion dissolves the oxide contours between the flattened structures and decreases the compactness of the coating surface. Thereafter, cracks appear on the coating under the physical impact of quartz particles in the erosion-corrosion process, which increases the tunnels for chloride ions entering the coating and further aggravates the corrosion effect.
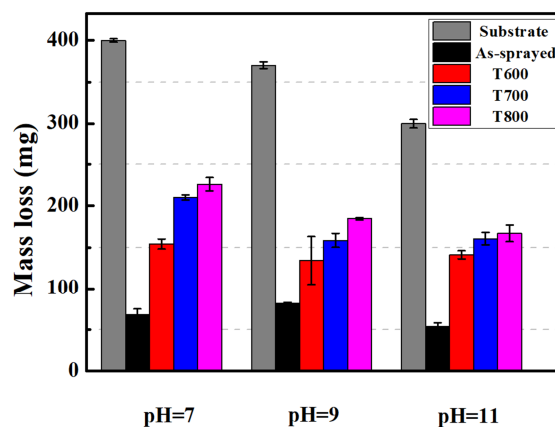
Fig. 12 Mass loss of the substrate, as-sprayed and heat-treated coatings after erosion-corrosion test in

alkalinity sand-containing NaCl slurry
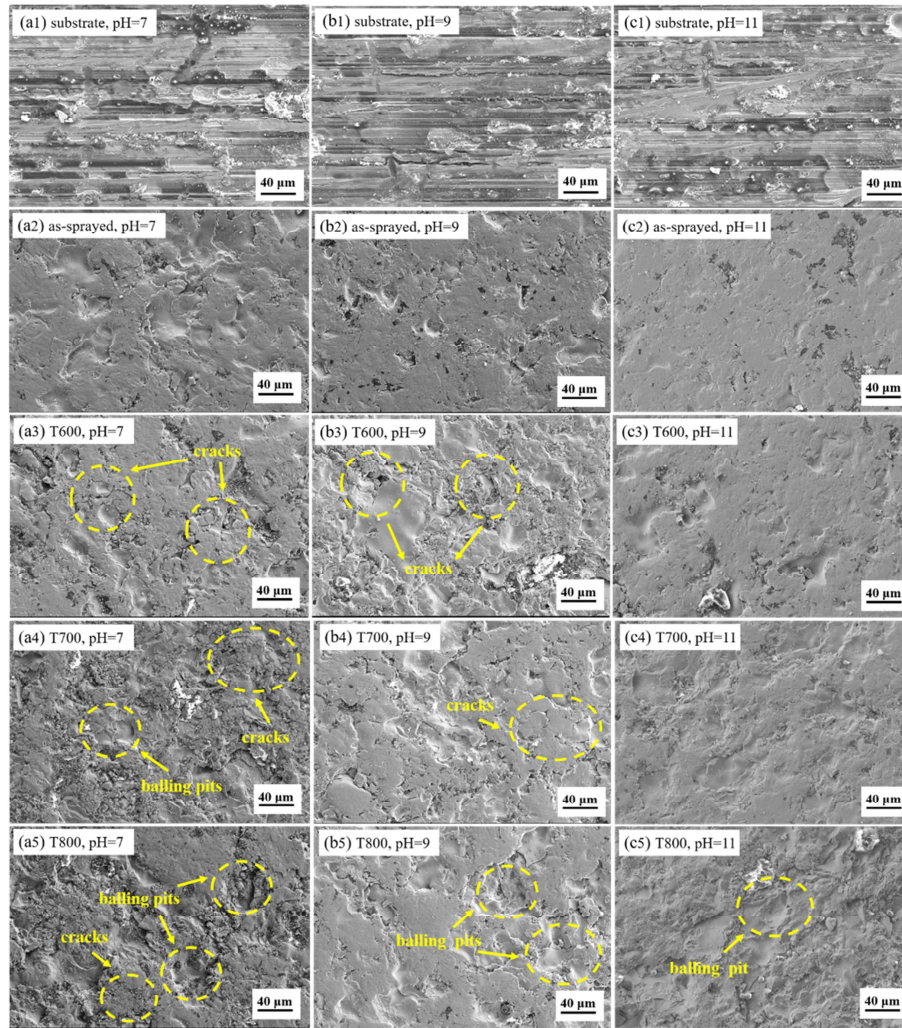
Fig. 13 SEM images of surface morphology of samples after erosion-corrosion test

VHT can increase the hardness of the coating due to the crystallization of amorphous

structure (Fig. 7), which makes the coating have better resistance to physical impact. However,

it reduces the corrosion resistance of the coating (Fig. 11). Compared with the advantages of

hardness increase caused by crystallization, the reduced corrosion resistance caused by

crystallization has a greater impact on the erosion−corrosion performance.

The pH value of slurry also has influence on erosion−corrosion behavior. The mass loss

of the sample treated at the same temperature tends to decrease with the pH values increasing.

This is due to the fact that the amorphous alloys ($Fe_{48}Cr_{15}Mo_{14}C_{15}B_6Y_2$ at.%) and 35CrMo

17

tend to form poorly soluble hydroxides or oxides in alkaline solutions that have a protective effect on the coatings. Previous studies also have shown that the dissolution rate of the oxide film will be reduced with the increase of pH due to the more stable performance of iron oxides in alkaline solutions [37].

4. Conclusion

$Fe_{48}Cr_{15}Mo_{14}C_{15}B_6Y_2$ amorphous alloy coatings were fabricated by HVAF, and the Fe-based amorphous/crystalline composite coatings with different amorphous degrees were obtained by vacuum annealing at different temperatures. The effect of VHT on the hardness, electrochemical corrosion, and erosion−corrosion of the Fe-AACs has been investigated, and the main conclusions can be summarized as follows.

(1) After VHT, the hardness of Fe-AACs increases due to the homogenization of the composition, crystallization, and dispersion strengthening of crystals. When the coating was heat treated at 800°C, the crystallization process becomes more complete, and the main crystallization precipitates are $Fe_{23}(C,B)_6$, $Fe_{17}Y_2$, and $Al_{13}Fe_4$. The formation of hard phases in the coatings results in the increase of hardness. The Vickers microhardness of T800 exceeds 1000 $HV_{0.1}$.

(2) VHT improved the hardness of the Fe-AACs, which greatly improves the wear resistance of the coating. The wear mechanism of the coating after VHT did not change significantly, and both were oxidative wear.

(3) Crystallization and grain growth due to VHT increase the number of grain boundaries, which causes the channels of chloride ions entering into the coating to increase. Therefore, the corrosion resistance of the coating gets worse with the increase of VHT temperature.

(4) Compared with the hardness enhancement caused by crystallization, the degradation of the corrosion resistance caused by crystallization has a greater impact on the erosion performance. Hydroxyl ions in alkaline solution can promote the formation of a protective

film (poorly soluble hydroxides or oxides) on the coating and substrate, slowing down the

ingression rate of chloride ions and reducing the mass loss.

Acknowledgement

References

[1]   W.J. Bottaa, J.E. Berger, C.S. Kiminami, V. Roche, R.P. Nogueira, C. Bolfarini, Corrosion resistance of Fe-based amorphous alloys, Journal of Alloys & Compounds 586 (2014) 105-110.

[2]   F. Huang, J.J. Kang, W. Yue, Z.Q. Fu, L.N. Zhu, D.S. She, J. Liang, C.B. Wang, Corrosion Behavior of FeCrMoCBY Amorphous Coating Fabricated by High-Velocity Air Fuel Spraying, J. Therm. Spray Technol. 28 (2018) 842-850.

[3]   Y.Y. Zhou, G.Z. Ma, H.D. Wang, G.L. Li, S.Y. Chen, H.J. Wang, L. Ming, Fabrication and characterization of supersonic plasma sprayed Fe-based amorphous metallic coatings, Materials & Design 110 (2016) 332-339.

[4]   Q. Luo, Y.J. Sun, J. Jiao, Y.X. Wu, S.J. Qu, J. Shen, Formation and tribological behavior of AC-HVAF-sprayed nonferromagnetic Fe-based amorphous coatings, Surface & Coatings Technology 334 (2018) 253-260.

[5]   A. Inoue, F.L. Kong, Q.K. Man, B.L. Shen, R.W. Li, F. Al-Marzouki, Development and applications of Fe- and Co-based bulk glassy alloys and their prospects, Journal of Alloys & Compounds 615 (2014) 2-8.

[6] D. Li, X.Y. Chen, X.D. Hui, J.P. Wang, P.P. Jin, H. Li, Effect of amorphicity of HVOF sprayed Fe-based coatings on their corrosion performances and contacting osteoblast behavior, Surface & Coatings Technology 310 (2017) 207-213.

[7] K. Bobzin, M. Öte, T. Königstein, K. Dröder, H-W. Hoffmeister, G. Mahlfeld, T. Schläfer, Development of Novel Fe-Based Coating Systems for Internal Combustion Engines, J. Therm. Spray Technol. 27 (2018) 736-745.

[8] H. Zohdi, H.R. Shahverdi, S.M.M. Hadavi, Effect of Nb addition on corrosion behavior of Fe-based metallic glasses in Ringer's solution for biomedical applications, Electrochemistry Communications 13 (2011) 840-843.

[9] H.H. Yao, Z. Zhou, L. Wang, Z. Tan, D.Y. He, L.D. Zhao, Thermal Conductivity and Wear Behavior of HVOF-Sprayed Fe-Based Amorphous Coatings, Coatings 7 (2017) 173.

[10] R.Q. Guo, C. Zhang, Y. Yang, Y. Peng, L. Liu, Corrosion and wear resistance of a Fe-based amorphous coating in underground environment, Intermetallics 30 (2012) 94-99.

[11] S. Wang, Y. Li, X. Wang, S.C. Y, W. Zhang, Glass-forming ability, thermal properties, and corrosion resistance of Fe-based (Fe, Ni, Mo, Cr)-P-C-B metallic glasses, Journal of Non-Crystalline Solids 476 (2017) 75-80.

[12] L.M. Zhang, S.D. Zhang, A.L. Ma, H.X. Hua, Y.G. Zheng, B.J. Yang, J.Q. Wang, Influence of sealing treatment on the corrosion behavior of HVAF sprayed Al-based amorphous/nanocrystalline coating, Surface & Coatings Technology 353 (2018) 263-273.

[13] G. Bolelli, M. Bursi, L. Lusvarghi, T. Manfredini, V. Matikainen, R. Rigon, P. Sassatelli, P. Vuoristo, Tribology of FeVCrC coatings deposited by HVOF and HVAF thermal spray processes, Wear 394-395 (2018) 113-133.

[14] J.F. Zhang, M. Liu, J.B. Song, C.M. Deng, C.G. Deng, Microstructure and corrosion

behavior of Fe-based amorphous coating prepared by HVOF, Journal of Alloys & Compounds 721 (2017) 506-511.

[15] S.F. Guo, N. Li, C. Zhang, L. Liu, Enhancement of plasticity of Fe-based bulk metallic glass by Ni substitution for Fe, Journal of Alloys & Compounds 504 (2010) 78–81.

[16] G. Liu, Y. An, J. Chen, G.L. Hou, J. Chen, Erratum to: Influence of Heat Treatment on Microstructure and Sliding Wear of Thermally Sprayed Fe-Based Metallic Glass Coatings, Tribol. Lett. 47 (2012) 163-163.

[17] J.B. Cheng, Z.H. Wang, B.S. Xu, Wear and Corrosion Behaviors of FeCrBSiNbW Amorphous/Nanocrystalline Coating Prepared by Arc Spraying Process, J. Therm. Spray Technol. 21 (2012) 1025-1031.

[18] A. Kumar, R. Kumar, P. Bijalwan, M. Dutta, A. Banerjee, T. Laha, Fe-based amorphous/nanocrystalline composite coating by plasma spraying: Effect of heat input on morphology, phase evolution and mechanical properties, Journal of Alloys & Compounds 771 (2019) 827–837.

[19] Y. Wang, S.L. Jiang, Y.G. Zheng, W. Ke, W.H. Sun, J.Q. Wang, Effect of porosity sealing treatments on the corrosion resistance of high-velocity oxy-fuel (HVOF)-sprayed Fe-based amorphous metallic coatings, Surface & Coatings Technology 206 (2011) 1307-1318.

[20] L. Qiao, Y.P. Wu, S. Hong, J.F. Zhang, W. Shi, Y.G. Zheng, Relationships between spray parameters, microstructures and ultrasonic cavitation erosion behavior of HVOF sprayed Fe-based amorphous/nanocrystalline coatings, Ultrasonics Sonochemistry 39 (2017) 39-46.

[21] J.M. González, F.Quintero, J.E. Arellano, R.L. Márquez, C. Sánchez, D. Pernía, Effects of interactions between solids and surfactants on the tribological properties of water-based drilling fluids, Colloids Surf. A Physicochem. Eng. Asp. 391 (2011) 216-223.

[22] G.T. Burstein, K. Sasaki, The birth of corrosion pits as stimulated by slurry erosion, Corrosion Science 42 (2000) 841-860.

[23] M. Yasir, C. Zhang, W. Wang, Y.Z. Jia, L. Liu, Enhancement of impact resistance of Fe-based amorphous coating by Al_2O_3 dispersion, Materials Letters 171 (2016) 112-116.

[24] J. Wu, S.D. Zhang, W.H. Sun and J.Q. Wang, Influence of oxidation related structural defects on localized corrosion in HVAF-sprayed Fe-based metallic coatings, Surface & Coatings Technology, 335 (2018) 205-218.

[25] R.Q. Guo, C. Zhang, Q. Chen, Y. Yang, N. Li, L. Liu, Study of structure and corrosion resistance of Fe-based amorphous coatings prepared by HVAF and HVOF, Corrosion Science 53 (2011) 2351-2356.

[26] Y.P. Wu, P.H. Lin, G.Z. Xie, J.H. Hu, M. Cao, Formation of amorphous and nanocrystalline phases in high velocity oxy-fuel thermally sprayed a Fe–Cr–Si–B–Mn alloy, Mater.Sci.Eng.A 430 (2006) 34-39.

[27] Liu W-H, Shieu F-S, Hsiao W-T, Enhancement of Wear and Corrosion Resistance of Iron-based Hard Coatings Deposited by High-Velocity Oxygen Fuel (HVOF) Thermal Spraying, Surface & Coatings Technology 249 (2014) 24-41.

[28] Z.B. Zheng, Y.G Zheng, W.H. Sun, J.Q. Wang, Effect of heat treatment on the structure, cavitation erosion and erosion–corrosion behavior of Fe-based amorphous coatings, Tribology International 90 (2015) 393-403.

[29] K. Kishitake, H. Era, F. Otsubo, Thermal-sprayed Fe-10CM3P-7C Amorphous Coatings Possessing Excellent Corrosion Resistance, J. Therm. Spray Technol. 5 (1996) 476-482.

[30] V.A. Blagojević, D.M. Minić, T. Žák, D.M. Minić, Influence of Thermal Treatment on Structure and Microhardness of $Fe_{75}Ni_2Si_8B_{13}C_2$ Amorphous Alloy, Intermetallics 19 (2011) 1780-1785.

[31] Z.B. Zheng, Y.G. Zheng, W.H. Sun, J.Q. Wang, Effect of heat treatment on the structure, cavitation erosion and erosion-corrosion behavior of Fe-based amorphous coatings,

Tribology International 90 (2015) 393-403.

[32] A. Inoue, L. Arnberg, M. Oguchi, U. Backmark, N. Bäckström, T. Masumoto, Preparation of Fe-Cr-Mo-C amorphous powders and microstructure and mechanical properties of their hot-pressed products, Mater. Sci. Eng. 95 (1987) 101-114.

[33] J.F. Archard, Contact and rubbing of flat surfaces. J Appl Phys. 24 (1953) 981-988.

[34] W.B. Qin, Y.Y. Liu, W. Yue, C.B. Wang, G.Z. Ma, H.D. Wang, Infuence of Frictional Interface State on Tribological Performance of Sintered Polycrystalline Diamond Sliding Against Diferent Mating Materials, Tribol. Lett. 67 (2019) DOI:10.1007/s11249-019-1196-1

[35] C. Zhang, L. Liu, K.C. Chan, Q. Chen, C.Y. Tang, Wear behavior of HVOF-sprayed Fe-based amorphous coatings, Intermetallics 29 (2012) 80-85.

[36] F. Otsubo, H. Era, K. Kishitake, Formation of Amorphous Fe-Cr-Mo-8P-2C Coatings by the High Velocity Oxy-Fuel Process, J. Therm. Spray Technol., 9 (2000) 494-498.

[37] C.-OA Olsson, D. Landolt, Passive films on stainless steels-chemistry, structure and growth, Electrochim. Acta 48 (2003) 1093-1104.

Highlights

- After VHT, the hardness of Fe-AACs increases. The microhardness of T800 exceeds 1000 $HV_{0.1}$.

- VHT improved the hardness of the Fe-AACs, but the corrosion resistance is getting worse. The wear resistance of the coating becomes better.

- Compared with the hardness enhancement caused by crystallization, the degradation of the corrosion resistance caused by crystallization has a greater impact on the erosion performance.

Declaration of interests

☒ The authors declare that they have no known competing financial interests or personal relationships that could have appeared to influence the work reported in this paper.

☐The authors declare the following financial interests/personal relationships which may be considered as potential competing interests: